JOURNAL OF SPACECRAFT AND ROCKETS
Vol. 33, No. 5, September–October 1996

Orbital Re-Entry Experiment Vehicle Ground and Flight Dynamic Test Results Comparison

Takashi Yoshinaga,* Atsushi Tate,† and Mitsunori Watanabe‡
National Aerospace Laboratory, Chofu-City, Tokyo 181, Japan
and
Takayuki Shimoda§
National Space Development Agency, Minatoku, Tokyo 107, Japan

The angular motion of an orbital re-entry experiment (OREX) vehicle model was tested in a transonic wind tunnel using a single-degree-of-freedom test method to investigate the angular motion of the OREX vehicle. The purpose of the OREX is to test heat shield materials and to obtain measurements of an aerodynamically heated flowfield. Approximate static and dynamic derivatives of the model were measured by a local linear curvefitting method. The angular motion of real OREX flight data was compared with the wind-tunnel test results. The maximum amplitude of the OREX vehicle in the transonic region is almost the same as that obtained in the wind-tunnel test.

Nomenclature

A = altitude, km
C_m = pitching moment coefficient, $M/qSD = I\theta''/qSD$
$C_{m\theta}$ = pitching moment curve slope, 1/rad
$C_{m\theta'}$ = damping-in-pitch derivative, $C_{mq} + C_{m\alpha} = (2IV_\infty/D)(\partial\theta''/\partial\theta')$, 1/rad
D = diameter, reference length
d = diameter of sting
f = frequency of oscillation, Hz
I = moment of inertia, I_{yy} or I_{zz}
M = moment of force, $I\theta''$
M_∞ = Mach number
q = dynamic pressure, $\frac{1}{2}\rho V_\infty^2$
R = radius, m
Re_∞ = Reynolds number, DV_∞/ν_∞
S = reference area, $\pi(D/2)^2$, m^2
T = period, s
t = time, s
V_∞ = velocity, m/s
α = angle of attack
β = angle of sideslip
θ = angle of incidence, deg, rad
θ' = angular velocity of incidence
θ'' = angular acceleration of incidence
σ = angle of bank

Introduction

FOR the purpose of testing heat shield materials for the future winged re-entry vehicle HOPE and for the purpose of studying the characteristics of an aerodynamically heated flowfield, the orbital re-entry experiment (OREX) vehicle, as illustrated in Fig. 1a, was launched by an H-II rocket.[1] By successfully re-entering the atmosphere from space, the OREX became Japan's first re-entry vehicle. As in Fig. 1b, the OREX vehicle separated from the rocket at an altitude of about 450 km. Then after completing one Earth orbit, it decelerated by means of a reverse jet and re-entered the atmosphere, traversing a black out region. After emerging from the black out region, the OREX vehicle transmitted flight and aerodynamic heating data to an aircraft and a ship in the vicinity. Except during certain periods of its flight path, the OREX vehicle controlled its attitude using thruster jets. When the OREX vehicle reached subsonic flight speed, it deployed a parachute, terminated attitude control, and splashed down into the sea.

As shown in Fig. 1a, the OREX vehicle has a spherical carbon/carbon nose cap and a conical section of diameter 3.40 m with an apex half-angle of 50 deg. Heat shield ceramic tiles cover the conical section surface reinforced by a honeycomb panel. The vehicle has a rounded outer edge of $R = 100$ mm. The rear of the vehicle is made up of a conical panel with an apex half-angle of 75 deg. The shape of the OREX vehicle was determined by means of static tests on several model shapes to maximize aerodynamic stability and by numerical calculation to reduce the heating rate in re-entry. The shapes included several blunted conical models with large half-angle

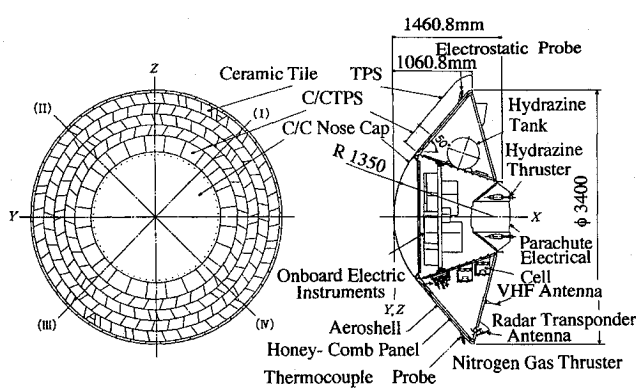

Fig. 1a Configuration of OREX.

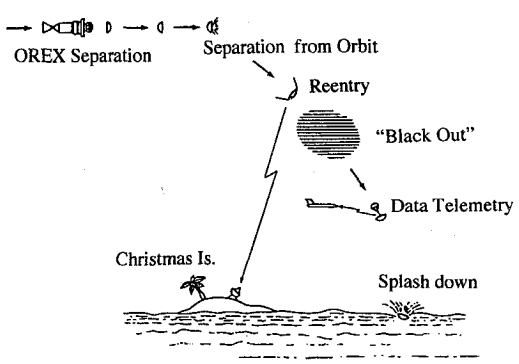

Fig. 1b Re-entry of OREX.

Received June 20, 1995; revision received May 6, 1996; accepted for publication May 10, 1996.

*Head, Aerodynamics Division, Supersonic Wind Tunnel Control Section. Member AIAA.
†Senior Researcher, Aerodynamics Division, Wind Tunnel Measurement Section.
‡Researcher, Aerodynamics Division, Wind Tunnel Control Section.
§Engineer, Space Recovery Systems Office.

of 45–55 deg, both with and without rounded edges. In addition, dynamic characteristics such as an angular motion were measured to predict cases of excessive pitching or coning that could result in divergence to tumbling for the flight vehicle. Supersonic wind-tunnel experiments on the OREX model using a single-degree-of-freedom (DOF) oscillation method revealed an increase in the amplitude of vehicle oscillations with a decrease in the Mach number approaching the transonic flight regime.

A survey of free oscillation and free-flight experimental data from ballistic ranges, which is used to simulate the re-entry of vehicles into the atmospheres of other planets, showed that the OREX-type models displayed coning motion of amplitude about 20 deg in the transonic region and a lower amplitude of oscillation at supersonic speeds,[2–9] thus supporting these measurements. The experiments to determine the maximum amplitude of oscillation of the OREX vehicle were conducted by the National Aerospace Laboratory (NAL) and the National Space Development Agency of Japan (NASDA) using single-DOF models in hypersonic, supersonic, transonic, and subsonic wind tunnels. The experiments illustrated a maximum oscillation of about 20 deg in the transonic region and much lower oscillations in the other flight regimes.

In this paper the experimental results of the transonic flow region are presented and compared with the actual angular motion of the OREX vehicle on its re-entry flight. Despite the fact that single-DOF oscillation tests on the sting in the wind tunnel do not exactly simulate real free flight,[8] the method yields similar characteristics to actual flight when the combined angular motion of pitching and yawing passes in the vicinity of 0 deg.

Models and the Transonic Wind-Tunnel Test

Single-DOF angular motion experiments were carried out on the OREX model using the 1 m × 1 m blowdown transonic wind tunnel at Kawasaki Heavy Industries in Gifu. As shown in Fig. 2a, the OREX model (a 1/30 scale) has a diameter of $D = 113.3$ mm with an edge radius of $R = 3.3$ mm. Two other models, one with an edge radius of $R = 2.0$ mm and another with a sharp edge of $R = 0.0$,

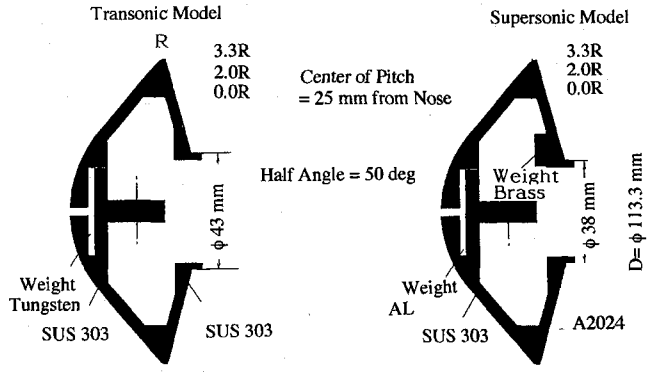

Models	Transonic	Supersonic
Weight (g)	773.9	682.1
Moment of Inertia I (g cm^2)	7.09×10^3	5.32×10^3

Fig. 2a OREX models in transonic and supersonic wind tunnel.

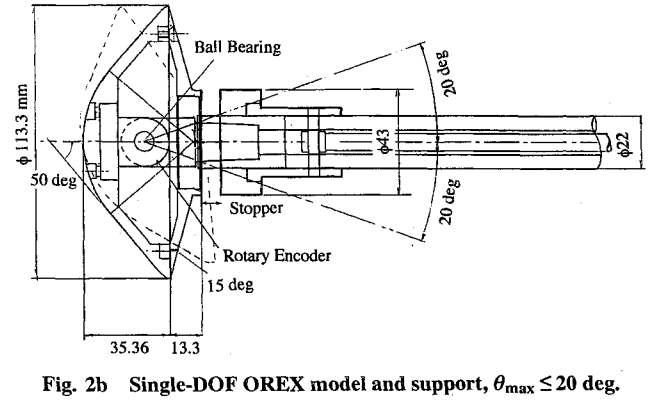

Fig. 2b Single-DOF OREX model and support, $\theta_{max} \leq 20$ deg.

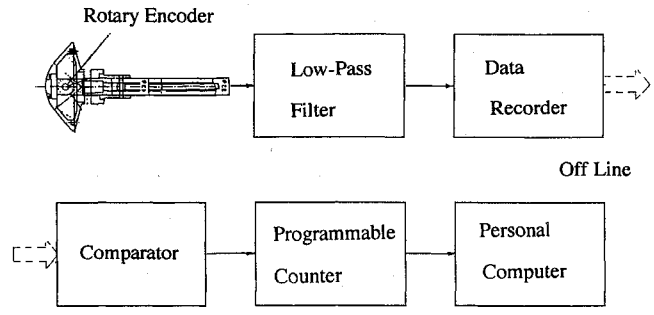

Fig. 3 Data processing diagram of angle of incidence $\theta(t)$.

were also tested. The forward components of the models were made from stainless steel, SUS 303, and were balanced by weights made from tungsten, aluminum, and brass to create the proper center of gravity near the center of rotation.

Figure 2b shows a model installed on a single-DOF test sting ($d = 22$ mm) with its two ball bearings. No spring was used in the model to react to the aerodynamic force. The moment of inertia of the model was selected such that the nondimensional equation of angular motion almost matched that of the full-scale OREX vehicle. To remove the gravitational effects, the model was mounted such that the single-DOF of motion was a yaw angle in the horizontal plane. The mechanical limit of the yaw amplitude was 20 deg. For the sake of convenience, the angle of yaw is expressed as an angle of incidence θ. During the experiments, the model was held in place using a pneumatic cylindrical stopper until transonic flow had settled in the test section. The models were then released from $\theta = 0$ deg, allowed to move freely during the experiment, and then stopped and re-released using the pneumatic cylinder two to three times during each run of the wind tunnel.

Figure 3 shows the data acquisition process used in the experiments. The variation of the angle of incidence θ was measured using an incremental rotary encoder that produced two sinusoidal signals with a 90-deg phase shift. The signals, once stored in the data recorder, were sent to a quadratic accurate programmable board on a personal computer to transform into the variation of the angle of incidence $\theta(t)$ with an accuracy of 0.25 deg. The angles were sampled at intervals of $\Delta t = 2.5$ ms. Then, from the quasisteady limit cycle data and the frequency, the maximum amplitude of oscillation and the static stability coefficient were measured. Finally, using the data of the buildup process to the limit cycles, the dynamic stability for each condition was examined.

Experimental Results

Variation of Angles of Incidence with Time

In Fig. 4, the variations of the incidence angle with time $\theta(t)$ for the OREX model are shown for the conditions $0.7 \leq M_\infty \leq 1.4$. When the stopper was pulled back in a transonic flow, the model began to oscillate and the amplitude increased and decreased randomly for about 10 s. Then the stopper was pushed forward again to stop the oscillation. For $M_\infty = 0.95$ at $Re_\infty = 2.21 \times 10^6$ (Fig. 4d), the model oscillated over the region $0 < \theta(t) < 11$ deg. Under the condition $M_\infty \geq 1.0$, the amplitude was found to increase more rapidly than for $M_\infty \leq 0.9$. As shown in Fig. 4e, for $M_\infty = 1.0$ at $Re_\infty = 2.25 \times 10^6$, the model began to oscillate with increasing amplitude until it reached a maximum value within 2 s. The amplitude of oscillation then varied between 19 and 11 deg with an average of 16 deg. This nonlinear angular oscillation illustrates that for this flow condition a recovering moment to $\theta = 0$ deg is acting on the model, showing that the motion is statically stable, $\partial\theta''/\partial\theta < 0$, but dynamically unstable, $\partial\theta''/\partial\theta' > 0$. At Mach numbers $0.95 \leq M_\infty \leq 1.4$, the OREX model and its modified models oscillated with an unsteady amplitude of θ, representing an unsteady limit cycle. A dynamically unstable moment, $\partial\theta''/\partial\theta' > 0$, acts in the amplitude increasing periods, whereas a dynamically stable moment, $\partial\theta''/\partial\theta' < 0$, acts in the amplitude decreasing periods. In these cases, therefore, dynamic stability varies even within the limit cycle region.

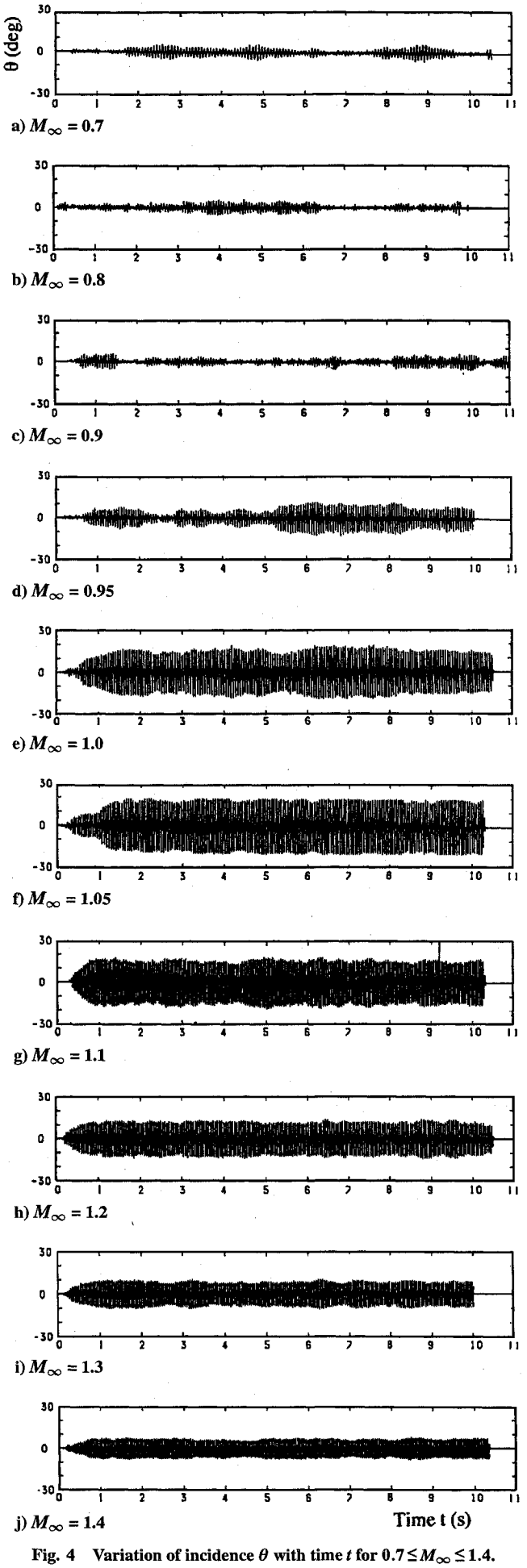

Fig. 4 Variation of incidence θ with time t for $0.7 \leq M_\infty \leq 1.4$.

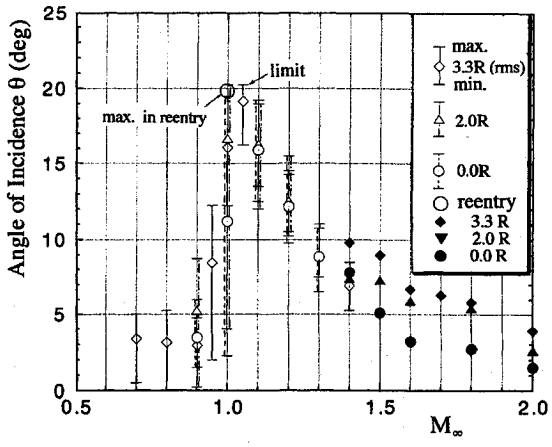

Fig. 5 Variation of mean angles of incidence θ with Mach number M_∞ for OREX models with various edge radius.

Variation of Amplitude θ with Mach Number M_∞

Plotted in Fig. 5 is the rms angle of incidence θ as a function of M_∞ with maximum and minimum values of the OREX model between 2 and 10 s after the model was set free to yaw. Near $M_\infty = 0.9$, the amplitude begins to increase, and at $M_\infty = 0.95$, the model shows a large variation of amplitude with time. Oscillations of about 20 deg, the maximum angle allowed by the model support sting, occur at $M_\infty = 1.05$. At this condition the model often collided against the sting. With a further increase in M_∞, the amplitude decreases, and at $M_\infty = 1.4$, it is less than 10 deg. For the increase of the Reynolds number, amplitude tends to decrease.

Also shown in Fig. 5 are the mean values of maximum and minimum angles of incidence for the OREX model and two other modified models tested in the NAL 1 m × 1 m supersonic wind tunnel. In the supersonic region, the model edge shape affects the magnitude of the amplitude more than at lower M_∞. The sharp-edged model ($R = 0.0$ mm) shows a smaller amplitude than the OREX model ($R = 3.3$ mm). This observation differs from the previously observed results.[4]

At $M_\infty = 1.4$, a difference exists in the amplitudes of oscillation between the supersonic and transonic wind-tunnel experiments. This difference is explained by the difference in size of the stoppers used in both experiments. To allow for a higher maximum amplitude of oscillation ($\theta_{max} = 20$ deg) in the transonic experiments, a stopper of diameter 43 mm was used, as shown in Fig. 2a. For the supersonic experiments the stopper used was 38 mm in diameter ($\theta_{max} = 15$ deg).

Trajectories on Phase Planes

To analyze the angular motions observed in the transonic wind-tunnel experiments, the angles of attack $\theta(t)$ (Fig. 6a) were differentiated twice with respect to time to obtain $\theta'(t)$ and $\theta''(t)$ (Figs. 6b and 6c). The value of $\theta''(t)$ is proportional to the moment acting on the model. Figures 6d, 6e, and 6f are plots of these same data in the form (θ, θ'), (θ, θ''), and (θ', θ''), respectively, with time t as the parameter. The trajectory in Fig. 6d does not converge to a single limit cycle after starting from the origin ($\theta = 0, \theta' = 0$), The trajectory of the data sometimes crosses the cycles of previous data. This fact means that, in the buildup of a limit cycle oscillation, the moment does not act as a single-value function of (θ, θ'). However, because the trajectory does not cross at a large angle, the dynamic moment of force does not change randomly to a large scale.

Figure 6e corresponds to the variation of the moment of force M with θ acting on the model since $M = I\theta''$. Because this figure illustrates a thin, straight, and roughly constant slope ($\partial\theta''/\partial\theta = \text{const}$) of the trajectory, the static moment curve slope $C_{m\theta}$ is almost constant for a wide range of θ, where the local static moment curve slope can be represented as $C_{m\theta} = I(\partial\theta''/\partial\theta)/(qSD)$. In other words, the static moment coefficient can be approximated as a linear function of θ over a wide range of angular motion, $-18 \leq \theta \leq 18$ deg, as $C_m = C_{m\theta}\theta$. In the present expression of the moment, the frictional moment as a result of the ball bearings, M_f is included as $M = M_a + M_f = I\theta''$, where M_a is the aerodynamic moment. The frictional moment M_f is negative in proportion to θ'. We assume

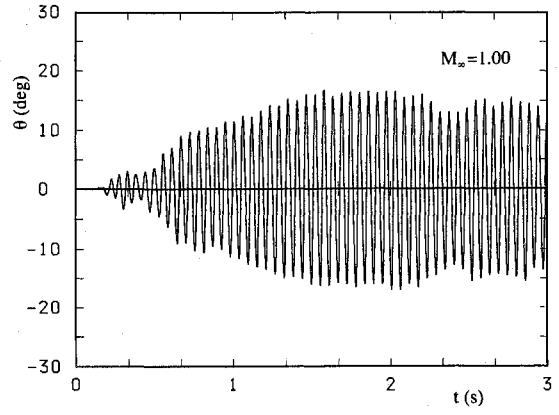

Fig. 6a Variation of θ with time t for OREX model.

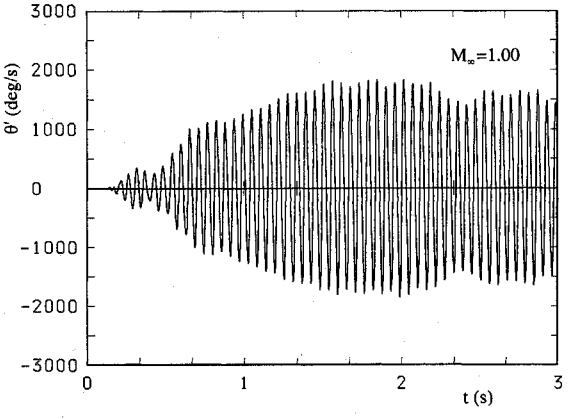

Fig. 6b Variation of θ' with time t for OREX model.

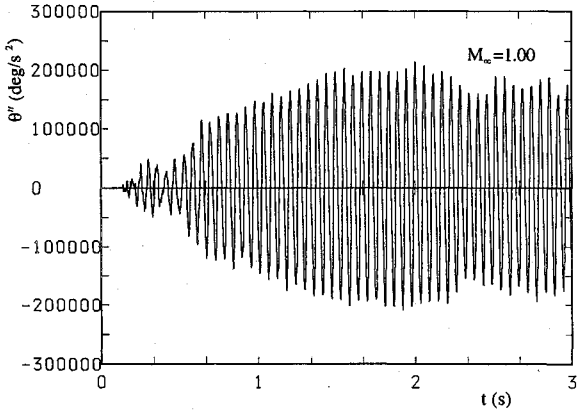

Fig. 6c Variation of θ'' with time t for OREX model.

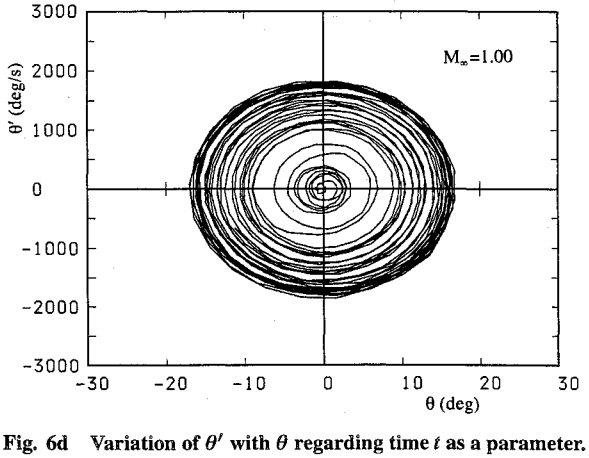

Fig. 6d Variation of θ' with θ regarding time t as a parameter.

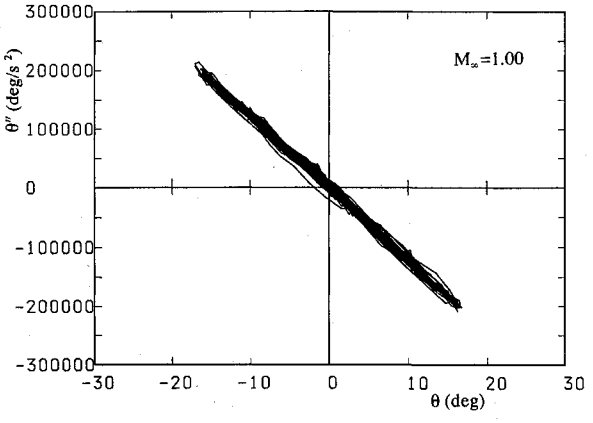

Fig. 6e Variation of θ'' with θ regarding time t as a parameter.

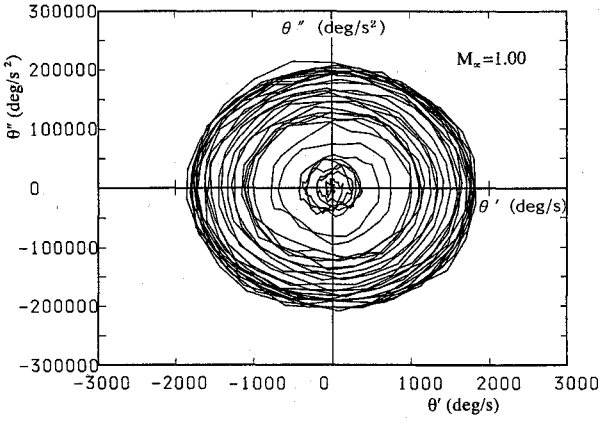

Fig. 6f Variation of θ'' with θ' regarding time t as a parameter.

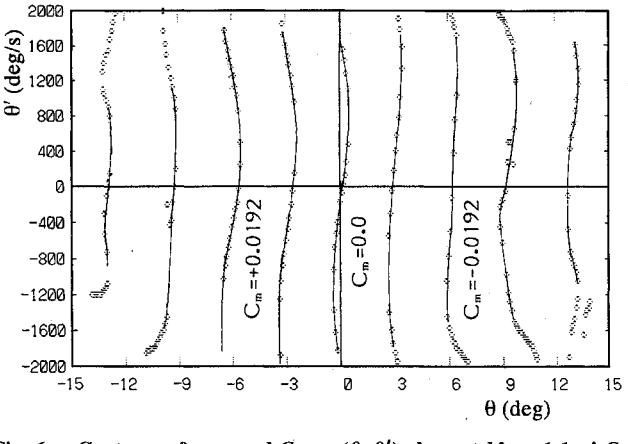

Fig. 6g Contours of averaged C_m on (θ, θ') plane at $M_\infty = 1.1$; $\Delta C_m = 0.0096$.

that the aerodynamic moment M_a is very great in comparison to the frictional moment M_f.

Moment of Force Acting on the OREX Model

The moment of force acting on the OREX model is shown in Fig. 6c as $I\theta''(t)$. In the analysis of autorotations of rocket-like bodies and two-dimensional wings and the wing rock of a delta wing using the phase plane method,[10–12] the moment of force $I\theta''$ is a typical single-value function of (θ, θ'). In other words, the trajectory draws a curved surface as a function of (θ, θ') without crossing over itself. In the present oscillation on the buildup of the limit cycle in Figs. 6a and 6d, the amplitude increased and sometimes decreased, showing that the moment is not a clear single-value function of (θ, θ'). By curvefitting the crossing points of the trajectories passing through a plane at $\theta = \theta_n$ parallel to the (θ', θ'') plane using a single curve polynomial of θ', an averaged curve of the moment force $M = I\theta''$ has been defined. Therefore, polynomials for M,

at every 0.1 deg in the range $-14 \leq \theta \leq 14$ deg, can be found. Using these polynomials, the contours of the moment coefficient $C_m(\theta, \theta')$ are plotted on the phase plane in Fig. 6g for $M_\infty = 1.1$, where the experimental data for two buildups to the limit cycle for the same condition were used. The difference between the contours is $\Delta C_m = 0.0096$. By comparing the distance between the contour curves, the slope near the origin is larger than it is further along the θ axis. In the θ' direction from the origin, the moment increases but again decreases to zero in the limit cycle region.

Derivatives of the Moment Coefficients

Initially, assume a linear expression for the moment of force M of angular oscillation as follows:

$$M = I\theta'' = qSD[C_{m\theta}\theta + (C_{mq} + C_{m\alpha'})(D/2V_\infty)\theta'] \quad (1)$$

where the suffix q of C_{mq} is the pitching rate of a body. Assuming that the solution to this equation is $\theta = \theta_0 \exp(\mu t) \sin \omega t$, the derivatives are then written as

$$C_{m\theta} = -\frac{I(\mu^2 + \omega^2)}{qSD} \cong -\frac{I\omega^2}{qSD} \quad (2)$$

$$C_{m\theta'} = C_{mq} + C_{m\alpha'} = (4I/SD^2)(V_\infty/q)\mu \quad (3)$$

where $\omega = 2\pi f$.

Next, we will examine the experimental results using an equation similar to the one shown; however, it includes a nonlinear term.

Pitching-Moment-Curve Slope $C_{m\theta}$

Although the angular oscillation in the transonic experiments was nonlinear, $\partial\theta''/\partial\theta$ was practically linear throughout the entire experiment in the whole range of θ except near the origin. Therefore, by measuring the frequency of oscillation f, $C_{m\theta}$ can be calculated using Eq. (2). Figure 7 illustrates the variation of $C_{m\theta}$ with the Mach number, showing a minimum value at $M_\infty = 1.05$. To examine the effect of the Reynolds number, the model was tested for increased values of the Reynolds number at $M_\infty = 1.1$ and 1.2. For the increase of Reynolds number, $C_{m\theta}$ increases, but the differences in $C_{m\theta}$ in these cases were found to be small. The term $C_{m\theta}$ can also be obtained using the relation

$$C_{m\theta} = I\left(\frac{\partial\theta''}{\partial\theta}\right)\Big/(qSD) \quad (4)$$

by measuring the slope of $\partial\theta''/\partial\theta$ such as that of Fig. 6e. Both methods were found to yield almost the same values of $C_{m\theta}$.

Damping-in-Pitch Derivative $C_{mq} + C_{m\alpha'}$

The damping-in-pitch derivative is defined near the origin as

$$C_{m\theta'}(= C_{mq} + C_{m\alpha'}) = \left.\frac{\partial C_m(\theta, \theta')}{\partial\theta'}\right|_{\theta=0,\theta'=0} = \left.I\frac{\partial\theta''}{\partial\theta'}\Big/(qSD)\right|_{\theta=0,\theta'=0} \quad (5)$$

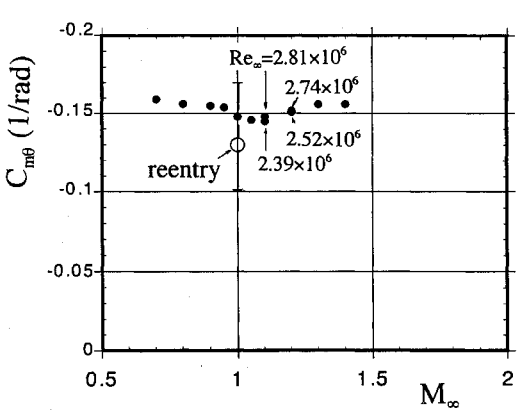

Fig. 7 Pitching-moment-curve slope $C_{m\theta}$ with M_∞ for OREX model.

Equation (3) yields $C_{mq} + C_{m\alpha'} = \text{const}$ at $\theta = 0$ where the linear negative damping moment acts. However, it is only a good estimate in the vicinity of $\theta = 0$ and $\theta' = 0$. For the present oscillation, a nonlinear unsteady positive and negative damping moment acts from $\theta = 0$ to the limit cycle. As shown in Fig. 6e, the variation of $C_m(\theta, \theta')$ in the θ' direction is not as large. If an oscillation is linear, its trajectory in phase space $(\theta, \theta', \theta'')$ will be on a plane with an inclined angle $\partial\theta''/\partial\theta = \text{const}$ in the θ direction and with an inclined angle $\partial\theta''/\partial\theta' = \text{const}$ in the θ' direction passing through the origin of phase space.

One of the methods used to analyze such a nonlinear oscillation is the local linear fitting method, where a part of a nonlinear oscillation trajectory is fitted by a linear angular oscillation. When a trajectory in phase space passes through points $(\theta_A, \theta'_A = 0, \theta''_A)$ on the (θ, θ'') plane, $(\theta_B = 0, \theta'_B, \theta''_B)$ on the (θ', θ'') plane, $(\theta_C, \theta'_C = 0, \theta''_C)$ on the (θ, θ'') plane, and so on, a plane is defined such that it includes three points: the origin, the point $(\theta_A, \theta'_A = 0, \theta''_A)$, and $(\theta_B = 0, \theta'_B, \theta''_B)$. Then the plot curve from $(\theta_A, \theta'_A = 0, \theta''_A)$ to $(\theta_B = 0, \theta'_B, \theta''_B)$ will be almost included in the plane. To specify such a plane, the slope θ''_A/θ_A in the θ direction is defined, which corresponds to

$$\frac{I(\theta''_A/\theta_A)}{qSD} \cong C_{m\theta}(\theta_A) = \left(\frac{\partial\theta''}{\partial\theta}\right)\Big/qSD\Big|_{\theta=\theta A,\theta'=0} \quad (6)$$

as a function of θ. This value is also regarded as a function of θ_B. The slope θ''_B/θ'_B in the θ' direction is defined, which corresponds to

$$\frac{I(\theta''_B/\theta'_B)}{qSD} \cong C_{m\theta'}(\theta'_B) = I\left(\frac{\partial\theta''}{\partial\theta'}\right)\Big/qSD\Big|_{\theta=0,\theta'=\theta B} \quad (7)$$

as a function of θ'_B for the locally linearly approximated plane.

These values are plotted in Figs. 8a of $C_{m\theta}(\theta)$ and 8b of $C_{m\theta'}(\theta')$ for $M_\infty = 0.9$ and Figs. 8c and 8d for $M_\infty = 1.0$. For $M_\infty = 0.9$, Fig. 8a shows that $C_{m\theta}$ is not constant and varies in the region $-6 \leq \theta \leq 6$ deg. Figure 8b shows $C_{m\theta'}(\theta')$ is large near the origin in positive and negative damping directions but becomes almost zero for large angular velocities θ'. For $M_\infty = 1.0$, Fig. 8c shows that $C_{m\theta}$ becomes constant except near the origin, where the values fluctuate. The $C_{m\theta}$ for large θ is the same as the one shown in Fig. 7. Figure 8d illustrates that near the origin the negative damping-in-pitch derivative ($0 < C_{m\theta'}$) is greater than the positive damping-in-pitch derivative, which occurs at random. As the angular velocity increases, $|C_{m\theta'}|$ rapidly becomes small in the limit cycle region.

Comparison of the Angular Motion of the OREX in Actual Flight with the Wind-Tunnel Experiments

Attitude Variation of the OREX

Figures 9a–9c show the variation of attitude angles for the OREX (angle of attack α, angle of yaw β, and angle of bank σ) as a function of time t after re-entering the atmosphere. As a general observation, from the plots of angles α and β, high-frequency variations are observed before deployment of the parachute and lower frequencies after deployment. Also in Fig. 10, data on the flight path such as altitude, velocity, and Mach number are plotted.

The attitude of the OREX vehicle was controlled with pulse thruster jets. The efficiency of the jets cannot be determined from the data, since the data were sent without knowledge of which was being used for control of the yaw and which for control of the angle of attack.

The high-frequency regions for the α and β data are plotted in more detail in Figs. 11a and 11b. The data do not show that the controls were sufficient to overcome the nonlinear dynamic moment to stop the oscillations.

On re-entry, OREX was rotated at $t = 7395$ s using its thruster jets about its x axis at a rate of roll equal to 18 deg/s as shown in Fig. 9c, after which at $t = 7520.7$ s the attitude control thruster jets for α and β began to function. From a comparison of Figs. 10, 11a, and 11b, it is apparent that the angular oscillations began at about $M_\infty = 3.3$. In spite of the control system being activated at this point, the amplitudes of α and β continued to increase. At $t = 7568.8$ s, in the transonic region of flight, the attitude controls were stopped

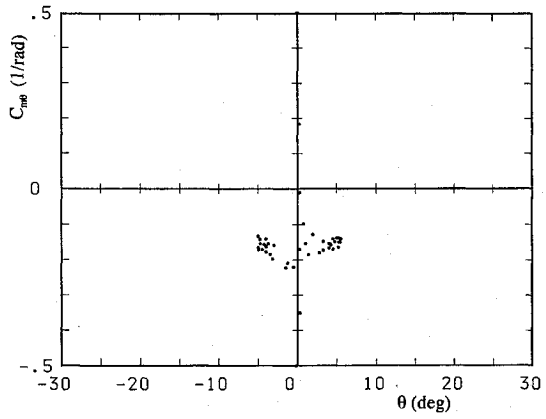

Fig. 8a Variation of $C_{m\theta}$ with θ by local linear method for $M_\infty = 0.9$.

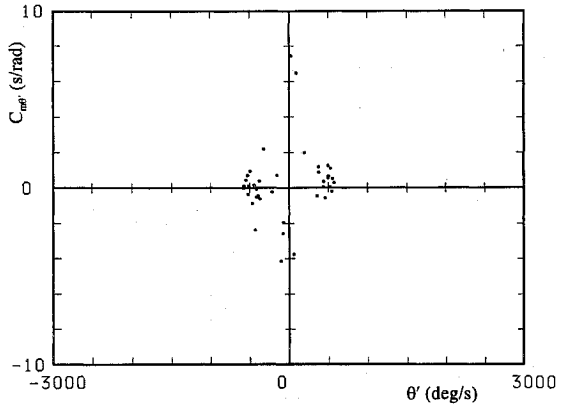

Fig. 8b Variation of $C_{m\theta'}$ with θ' by local linear method for $M_\infty = 0.9$.

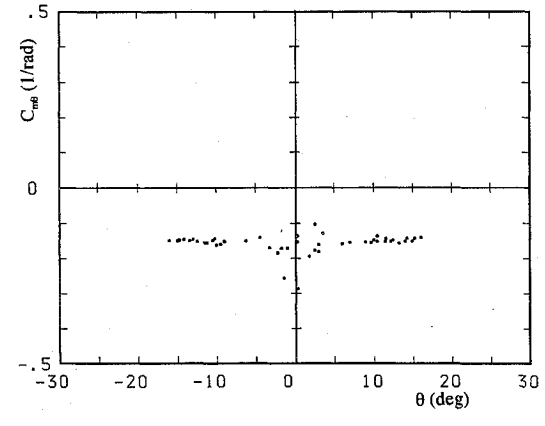

Fig. 8c Variation of $C_{m\theta}$ with θ by local linear method for $M_\infty = 1.0$.

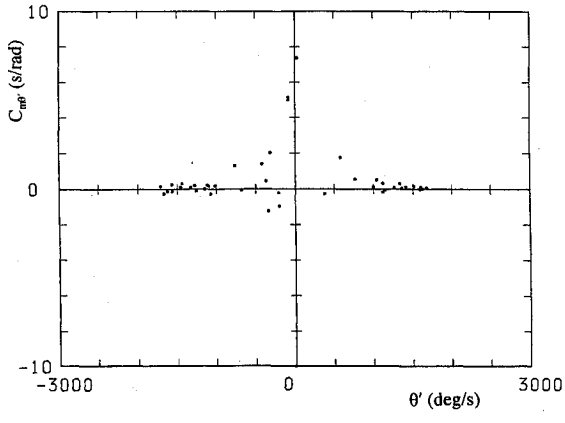

Fig. 8d Variation of $C_{m\theta'}$ with θ' by local linear method for $M_\infty = 1.0$.

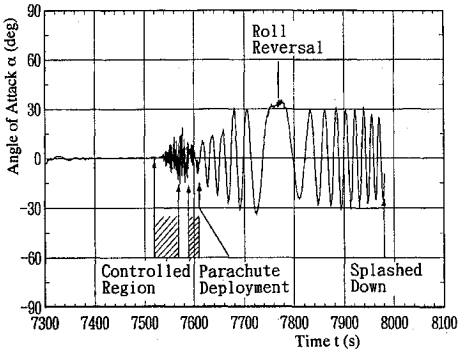

Fig. 9a Time history of angle of attack α of OREX after re-entering the atmosphere.

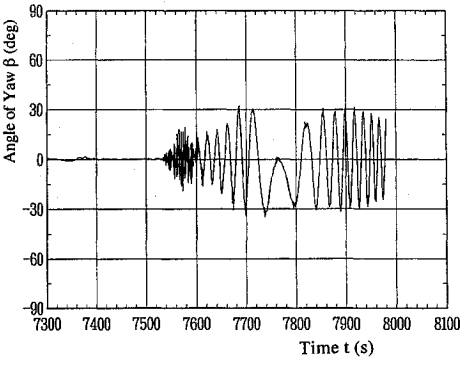

Fig. 9b Time history of angle of sideslip β of OREX after re-entering the atmosphere.

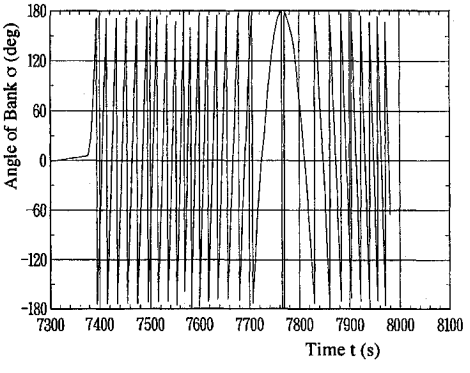

Fig. 9c Time history of angle of bank σ of OREX after re-entering the atmosphere with reversal of rolling.

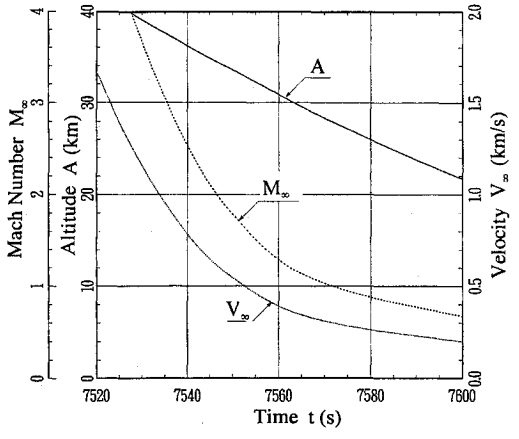

Fig. 10 Time history of altitude, velocity, and Mach number with respect to time.

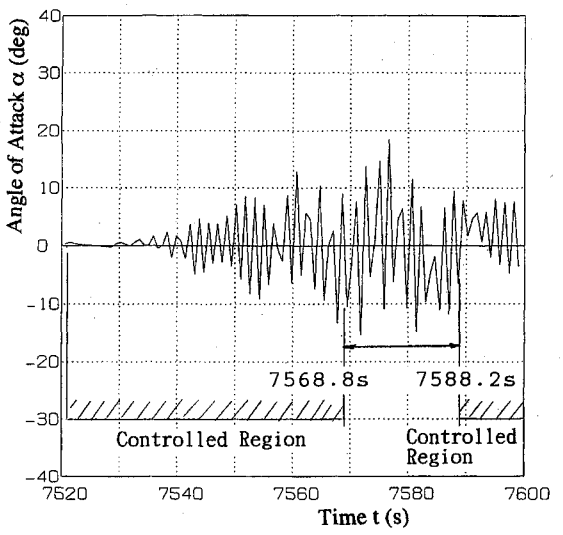

Fig. 11a Time history of α sampled every 0.8 s, including uncontrolled region.

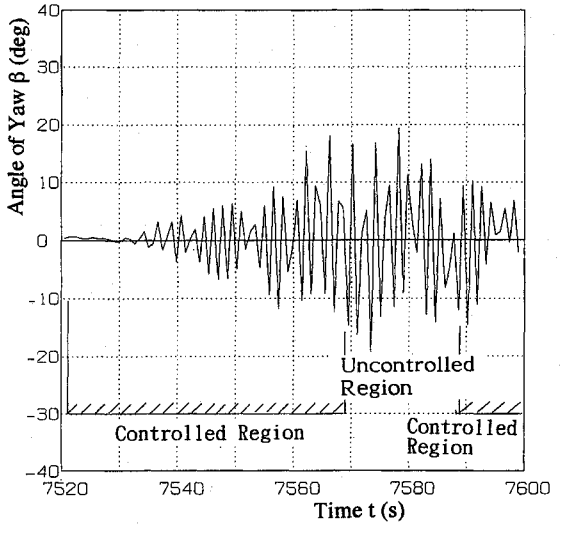

Fig. 11b Time history of β sampled every 0.8 s, including uncontrolled region.

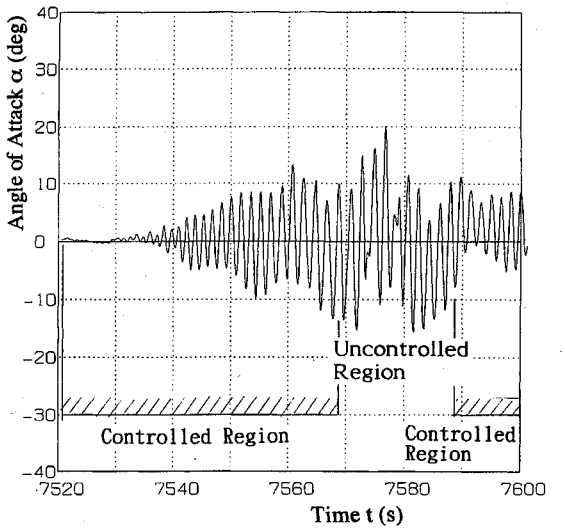

Fig. 12a Time history of α including uncontrolled region by Bezier curves.

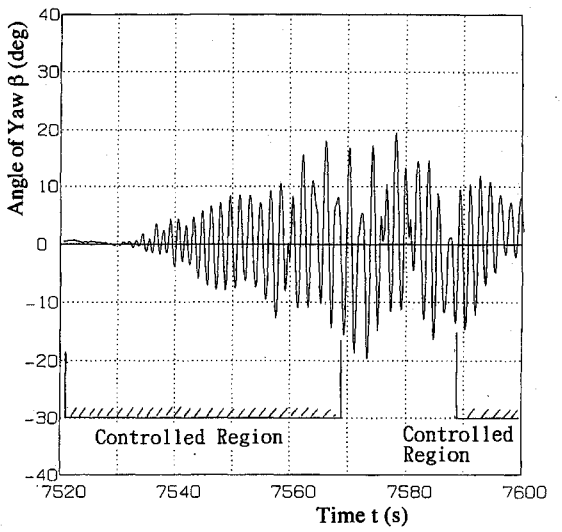

Fig. 12b Time history of β including uncontrolled region by Bezier curves.

when the angular velocities exceeded the preset limits of the control system. Later at $t = 7588.2$ s the controls were reactivated for a shorter period and then shut down when the parachute was deployed at $t = 7614.8$ s before OREX splashed down in the ocean.

During the pause in the controls in the transonic region, the amplitude of oscillation of the angles of attack and yaw reached their maximum values. The maximum amplitude observed in flight, about 20 deg, roughly coincides with the value observed in the wind-tunnel experiments. Note that after the deployment of the parachute the nominal amplitude of these angles increased by about twice. This seems to be a false amplitude caused by the measurement error of horizontal velocity.[1]

Reproducing of Attitude Angles with Bezier Curves

Finally, it is noted that the sampling period of the data is 0.8 s and the oscillations have a period of about $T = 2.0$ s (0.5 Hz). Usually in sampling theory the requirement for a continuous wave signal to be reproduced, including components of varying frequencies up to a frequency of f Hz, is that the signal must be sampled by a frequency greater than $2f$ Hz. A sampling period of 0.8 s (1.25 Hz), therefore, is not enough to reproduce the present unsteady oscillations with a shorter time period than 1.6 s.

Fortunately, in addition to the attitude angles of attack, yaw, and bank, data from the OREX also included the time derivatives of these angles, the angular velocities α', β', and σ'. Because the angular variation in a three-DOF system is affected by each of the other angular velocities, predicting the angular attitude between a sampled period is difficult. Assuming as a first step that the variation of each angle is approximately independent of the other angles, the angles were connected by a cubic curve using the angle and the angular velocity data sampled every 0.8 s at each point (Bezier curve).

Figures 12a and 12b are reshaped plots of the attitude angles α and β for the OREX, constructed using Bezier cubic curves as a function of time t including the uncontrolled region near $M_\infty = 1.0$. Figures 12a and 12b contain all of the data in Figs. 11a and 11b. In Figs. 11a and 11b the variation of amplitude is small between the periods where the sampled time coincides with the angles α and $\beta \cong 0$; however, for Figs. 12a and 12b larger amplitude variations appear. Based on these figures, the maximum amplitudes of α and β are estimated as about 20 deg with periods of about 2.0 s (0.5 Hz). These amplitude are similar to the values estimated by the wind-tunnel experiments. The maximum amplitude of the angle is shown in Fig. 5 as a circle. Using the frequency of $f = 0.5$ Hz, the static moment coefficient of OREX near $M_\infty = 1.0$ is estimated by Eq. (2) to be $C_{m\theta} = -0.130$. The absolute value of $C_{m\theta}$ for real flight is smaller than the value of $C_{m\theta} = -0.148$ measured in the wind-tunnel test at $M_\infty = 1.0$ shown in Fig. 7. Also, Fig. 13a is a plot of the variation of α and β from Figs. 11a and 12a with α as the horizontal axis and β as the vertical axis taking time t as a parameter. Figure 13b is a plot of the variation of α and β using the Bezier curves of plots in Figs. 12a and 12b, which gives a more realistic angular oscillation.

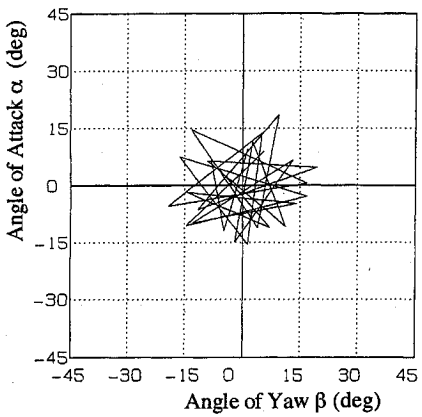

Fig. 13a Variation of attitude angles of α and β in uncontrolled region.

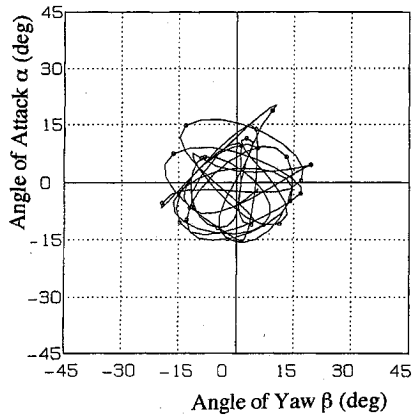

Fig. 13b Variation of attitude angles of α and β by Bezier curves in uncontrolled region.

Conclusions

To prevent tumbling of the OREX vehicle in the transonic region, a model test for a single-DOF angular oscillation was carried out in a transonic wind tunnel and the results were compared with the real flight data.

1) Flight data show that the OREX began angular oscillations of α and β in the region $M_\infty < 3.3$.

2) Transonic wind-tunnel experiments of an OREX model demonstrated that a damping and a negative damping moment acts for $M_\infty \leq 0.9$. For $M_\infty > 0.9$, a negative damping moment overcomes the damping moment, where a quasi-limit cycle oscillation was observed.

3) The model showed a maximum amplitude of $\theta \cong 20$ deg in the quasi-limit cycle oscillations at $M_\infty = 1.05$. During the transonic flight the OREX vehicle displayed almost the same amplitude of angular oscillation for α and β, while the attitude control was disengaged.

References

[1]NAL/NASDA HOPE Joint Study Team, "Reports of HOPE/OREX Workshop," edited by M. Mori, National Aerospace Lab., NAL SP-24, Tokyo, Japan, Sept. 1994.

[2]Krumins, M. V., "Drag and Stability of Mars Probe/Lander Shapes," *Journal of Spacecraft and Rockets*, Vol. 4, No. 8, 1967, pp. 1052–1057.

[3]Marco, W., "Dynamic Stability of High-Drag Planetary Entry Vehicles at Transonic Speeds," AIAA Paper 69-105, Jan. 1969.

[4]Sammonds, R. I., "Dynamics of High-Drag Probe Shapes at Transonic Speeds," NASA TN D-6489, Sept. 1971.

[5]Jaffe, P., "Dynamic Stability Tests of Spinning Entry Bodies in the Terminal Regime," *Journal of Spacecraft and Rockets*, Vol. 8, No. 6, 1971, pp. 575–579.

[6]Ericsson, L. E., "Re-Entry Capsule Dynamics," *Journal of Spacecraft and Rockets*, Vol. 8, No. 6, 1971, pp. 579–586.

[7]Jaffe, P., "Nonplaner Tests Using the Wind-Tunnel Free-Flight Technique," *Journal of Spacecraft and Rockets*, Vol. 10, No. 7, 1973, pp. 435–442.

[8]Steinberg, S., Uselton, B. L., and Siemers, P. M., III, "Viking Pitch-Damping Derivatives as Influenced by Support Interference and Test Techniques," *Journal of Spacecraft and Rockets*, Vol. 10, No. 7, 1973, pp. 443–449.

[9]Sammonds, R. I., and Kruse, R. L., "Aerodynamic Characteristics of the Planetary Atmosphere Experiments Test Entry Probe," *Journal of Spacecraft and Rockets*, Vol. 12, No. 1, 1975, pp. 22–27.

[10]Yoshinaga, T., Inoue, K., and Tate, A., "Determination of the Pitching Characteristics of Tumbling Bodies by the Free-Rotation Method," *Journal of Spacecraft and Rockets*, Vol. 21, No. 1, 1984, pp. 21–28.

[11]Yoshinaga, T., Tate, A., and Inoue, K., "Phase Plane Analysis for Non-Linear Oscillation of Bodies at High Angles of Attack," *IUTAM Symposium of Fluid Dynamics of High Angle of Attack*, edited by R. Kawamura and Y. Aihara, Springer–Verlag, Berlin, 1992, pp. 301–310.

[12]Yoshinaga, T., Tate, A., and Noda, J., "Wing Rock of Delta Wings with an Analysis by the Phase Plane Method," AIAA Paper 93-3684, Aug. 1993.

K. J. Weilmuenster
Associate Editor